Planetary and Space Science 253 (2024) 105983

Contents lists available at ScienceDirect

Planetary and Space Science

journal homepage: www.elsevier.com/locate/pss

The thermal impact of the self-heating effect on airless bodies. The case of Mercury's north polar craters

Pamela Cambianica [a,*], Emanuele Simioni [a], Gabriele Cremonese [a], Silvia Bertoli [a], Elena Martellato [a], Alice Lucchetti [a], Maurizio Pajola [a], Cristina Re [a], Adriano Tullo [a], Matteo Massironi [b]

[a] INAF Astronomical observatory of Padova, vicolo dell'Osservatorio 5, 35122, Padova, Italy
[b] Department of Geosciences, University of Padova, Via Giovanni Gradenigo 6, 35131, Padova, Italy

ARTICLE INFO

Keywords:
Mercury
BepiColombo
Thermal processes
Methods
Numerical

ABSTRACT

Thermal models are essential for studying airless planetary surfaces, as the interaction between topography and thermophysical properties plays a crucial role in determining a surface's response to localized illumination. Accurate temperature distribution calculations require a comprehensive investigation of sunlight scattering, a process that, despite its computational challenges, cannot be overlooked, especially when high resolution is necessary. Furthermore, thermal analysis is fundamental for assessing the stability of volatiles in polar regions. In this study, we introduce a novel approach by discretizing the Sun into 100 individual elements, allowing for a highly precise simulation of solar flux—an innovation crucial for accurately capturing temperature distributions in Mercury's polar craters, given the planet's proximity to the Sun. This level of discretization significantly enhances the accuracy of the thermal model, ensuring a more realistic depiction of how sunlight interacts with crater topography. We developed a dual-model approach that simulates both direct solar illumination and its scattering on two craters, Laxness and Fuller, located at Mercury's north pole. The illumination and thermal model predict temperature distribution and heat transfer based on the material's thermal properties and topography. The study examines the interaction between direct sunlight, causing localized heating, and scattered light, which influences the thermal response of surface materials. Detailed illumination maps and temperature profiles were generated over two Hermean years, revealing the significant impact of the self-heating effect on temperature distribution. The results show that specific regions experience indirect solar flux due to the craters' morphology, particularly in permanently shadowed regions (PSRs) that are heated exclusively by scattered radiation. Maximum temperature profiles for the Laxness and Fuller craters show a substantial temperature increase within PSRs compared to areas exposed to direct illumination. However, while self-heating does not affect the stability of water ice in the Laxness crater, in the Fuller crater, a section within the radar-bright material reaches temperatures of up to 210 K, potentially threatening the stability of water ice. Further investigation with the onboard SIMBIO-SYS instrument on the BepiColombo mission will help to better understand the current state of these craters and their volatile deposits.

1. Introduction

Space weathering processes, including solar wind, solar radiation, and micrometeorite impacts, represent the main drivers of surface alteration on airless bodies. The erosion of rocks, the degradation of craters, and the formation of regolith (Molaro and Byrne, 2012) are the direct consequences of thermal stress being the solar radiation the primary energy source on such bodies. When examining the impact of solar exposure on a surface, it is essential to consider two distinct mechanisms: thermal shock and thermal fatigue. Thermal shock occurs as an immediate response to abrupt temperature changes, leading to material failure and instantaneous fracturing due to the inability to adapt to sudden changes (Hall and Thorn, 2014). Conversely, thermal fatigue arises from repeated cycles of temperature variations, causing enduring damage on the material's structure. Such damage is intensified by the combined effects of differential expansion and thermal gradients, which produce internal stresses (Hall and Thorn, 2014).

Comprehending the illumination conditions and computing the radiative intensity on the surface of airless bodies are pivotal for assessing the effect of weathering caused by solar exposure.

* Corresponding author.
E-mail address: pamela.cambianica@inaf.it (P. Cambianica).

https://doi.org/10.1016/j.pss.2024.105983
Received 8 April 2024; Received in revised form 3 October 2024; Accepted 7 October 2024
Available online 11 October 2024

Thermal models play a crucial role in the study of rocky bodies, offering invaluable insights into their physical properties, thermal behavior, and evolutionary processes. By simulating the temperature distribution and heat transfer mechanisms within and on the surface of these bodies, thermal models enable to interpret observational data, predict future conditions, and understand the underlying thermal dynamics. These models are particularly important for bodies without significant atmospheres, where the effects of the thermal environment are directly influenced by solar radiation, surface composition, and topographical features. Furthermore, thermal models are fundamental in studying the thermal history of airless bodies, including their formation and cooling processes (Wakita and Minoru, 2011).

To accurately determine the surface and subsurface temperature distributions of an airless body, a thermophysical model must account for realistic physical conditions including topography, orbital parameters, surface roughness, and thermophysical properties such as thermal inertia. Moreover, it is essential to consider various insolation conditions on the surface, the direct solar radiation, including the solar limb darkening effect and obstructions by the local horizon, and the scattering of the nearby terrain (see Fig. 1). The initial step in developing an illumination and thermal model should prioritize the direct sunlight scenario on the body's surface, as it provides the most favorable signal-to-noise ratio (SNR) for observers (Filacchione et al., 2020). In such scenarios, areas of the surface exposed to the Sun are illuminated, while those beyond the local horizon remain in darkness. Accurately assessing the illumination conditions on a planetary surface also involves considering the shadows cast due to the Sun's apparent angular size as observed from the surface.

A point light source creates a simple shadow known as the umbra, typical for Solar System objects where the Sun's apparent diameter is small, resulting in the surface being illuminated by parallel rays. In contrast, an extended light source produces a more complex shadow comprising three distinct components: (i) the umbra, where no direct light from the source reaches; (ii) the penumbra, an area partially illuminated by the light source; and, (iii) the antumbra, where the occluding body is seen against the disk of the light source. Generally, for most Solar System objects, the Sun's apparent diameter is sufficiently small that the formation of a blurred penumbra around the central umbra is minimal. Nevertheless, for Mercury, the apparent size of the solar disk varies from 1.15° at aphelion to 1.76° at perihelion (Filacchione et al., 2020) due to its heliocentric distance. The incidence angle near Mercury's poles is close to 90°, causing the solar rays to graze the surface. Consequently, this leads to the Hermean surface being illuminated by diverging beams, creating a blurred transition zone between the umbra and penumbra, as illustrated in Fig. 2 of Filacchione et al. (2020).

In addition, topographic features and thermophysical characteristics significantly influence the scattering properties of a planetary surface by modifying local incidence and emission angles. In the analysis of temperature distribution on an airless surface, sunlight scattering must be accounted due to its contribution to the 'self-heating' effect. This phenomenon occurs when thermal radiation absorbed by topographic elements from sunlit areas warms the colder facets, thereby increasing the overall insolation absorbed by the surface (Yu and Ip, 2021). For instance, Rozitis et al. (2020) demonstrated that on the asteroid (101955) Bennu the amount of self-heating that occurred on the asteroidal hemispherical craters prevents water ice from being stable, thus giving a fundamental role to this effect in terms of radiative exchange of energy between surface elements. Although previous studies have considered scattering and self-heating, some have employed simplifying assumptions that streamline analytical calculations. Incorporating scattering and self-heating effects into thermophysical models presents a significant challenge due to the extensive computational time required to accurately estimate surface temperatures. In the literature, various methods have been adopted to reduce this computational time. For instance, Buhl et al. (1968)'s model of lunar surface temperatures omitted thermal re-radiation considerations. Paige et al. (1992) adopted a simplistic approach to thermophysical parameters, using constant, linear, or discontinuous methods. Jamsa et al. (1993) work on the thermal emission from rough surfaces overlooked heat conduction. Additionally, many models fail to account for actual topography, often simplifying impact craters as spherical sections, as noted by Paige et al. (1992) and Ingersoll et al. (1992). Vasavada et al. (1999) highlighted that, in such models, water ice remains stable for billions of years within Mercury's and the Moon's craters, although this idealized crater morphology might lead to incomplete outcomes. Only more recent research, such as that by Gläser and Gläser (2019), Scharringhausen and Witte (2020), Formisano et al. (2019, 2018), and Durga Prasad et al. (2022) include both scattering and re-radiation effects in their calculations.

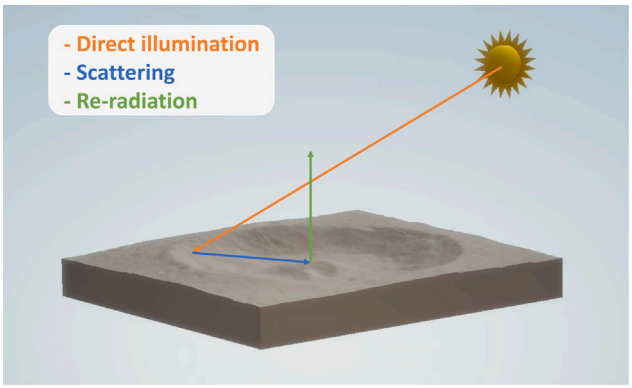

Fig. 1. Direct illumination (orange arrow), scattering (blue arrow), and re-radiation (green arrow) of the solar radiation in the case of an impact crater illuminated by an extended source at finite distance.

In this context, our study aims to quantify the thermal impact of incorporating scattering and self-heating effects into simulations of temperature distribution on airless surfaces. To achieve this, we have developed a ray-tracing illumination and thermal model that accurately represents the Sun's apparent position relative to the surface, allowing us to generate detailed radiative maps and temperature profiles for specific features on rocky surface. Our research differs from previous works, such as Formisano et al. (2018) and Durga Prasad et al. (2022), as we developed a custom tool for the entire analysis process, from crater illumination to temperature calculation. Given Mercury's proximity to the Sun, our tool includes a sophisticated approach to solar discretization (as explained in Section 3). Specifically, we do not consider the Sun as a point source but instead discretize it into 100 elements. This allows us to accurately model the influence of the Sun's apparent size on Mercury's surface, which is crucial for precise temperature calculations. This level of detail is particularly important for understanding the thermal dynamics within Mercury's permanently shadowed regions (PSRs). Additionally, our tool is designed for use in the context of the ESA's BepiColombo mission (Benkhoff et al., 2021), particularly for the SIMBIO-SYS instrument (Cremonese et al., 2020).

For this work, our focus is on two craters located in the northern polar region of Mercury, chosen for their distinct morphological characteristics that significantly influence the thermal dynamics within and for the presence of permanently shadowed regions. These craters, with their unique shapes, depths, and rim heights, offer valuable insights into the interplay between sunlight scattering, shadowing effects, and thermal behavior in extreme conditions. By examining these craters, we aim to enhance our understanding of the thermal processes at play in Mercury's polar regions, contributing to a more comprehensive model of planetary surface temperatures.

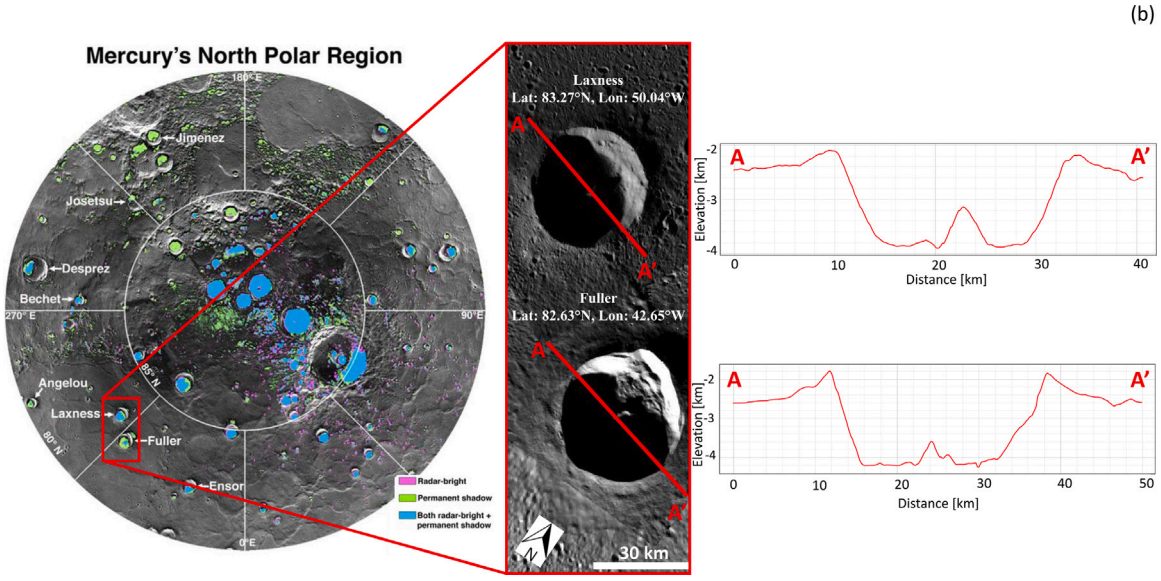

Fig. 2. Map of Mercury's north polar region with radar-bright-only regions (pink), regions of permanent shadow only (green), and regions that are both radar-bright and permanently shadowed (blue) (Deutsch et al., 2016) from Hamill et al. (2020), and topographic profiles of the Laxness (top right panel) and Fuller (bottom right panel) craters used in this work. Red lines (A–A') show the orientation of the extracted profile.

2. Target selection

We chose Mercury and its north polar impact craters due to their unique opportunity for examining the influence of crater morphology on self-heating effects. Impact craters near Mercury's poles are notable for their PSRs (Watson et al., 1961b,a), which are illuminated solely by scattered light and the thermal emission from the surrounding terrain, in addition to the internal heat of Mercury itself. Persistent bright features within these polar craters, suggestive of ice deposits (e.g. Harmon et al., 2011), were detected through Earth-based radar surveys conducted by the Arecibo Observatory and the MErcury Surface, Space ENvironment, GEochemistry, and Ranging (MESSENGER) spacecraft (Solomon et al., 2007), which found surface reflectance properties indicative of both water ice and other volatiles (e.g. Neumann et al., 2013; Chabot et al., 2014, 2016; Deutsch et al., 2016, 2018, 2017). Further analysis using Mercury Laser Altimetry (MLA) (Cavanaugh et al., 2007) data has led to models proposing that water ice and carbonaceous compounds could remain stable within PSRs for billions of years (Paige et al., 2013). Thus, the MESSENGER mission has significantly advanced our understanding of these deposits. However, the high-resolution detection, mapping, and compositional analysis of PSRs remain key objectives for the Spectrometer and IMagers for MPO Bepicolombo Integrated Observatory SYstem (SIMBIO-SYS, Cremonese et al., 2020) suite on ESA's BepiColombo mission (Benkhoff et al., 2021). This suite includes the STereo imaging Channel (STC, Cremonese et al., 2009), which will map Mercury's surface at a medium spatial resolution (at best 58 m/px); the High Resolution Imaging Channel (HRIC, Zusi et al., 2019), targeting approximately 20% of the surface at high resolution (pixel scale of about 5 m at 400 km from planet surface); and the Visible and near-Infrared Hyperspectral Imaging channel (VIHI, Capaccioni et al., 2009), which will provide global coverage at a spatial resolution of 120 m/px with spectral data. In this context, our selection of Mercury's north polar craters is pivotal to understanding the thermal behavior that affect the stability of various volatiles, such as water ice.

This, in turn, allows us to quantify the role of self-heating on the calculations of surface and subsurface temperatures by discretizing the Sun, contributing to the broader goal of characterizing Mercury's polar environments. This research focuses on the two polar craters on Mercury, named Laxness and Fuller, situated in the northern region of the Goethe Basin (refer to Fig. 2 and Table 1). These craters were chosen since data from the Goldstone/VLA Radar revealed the presence of radar-bright areas along the southern interior of both craters (Butler et al., 1991). The Mercury Dual Imaging System (MDIS) (Hawkins et al., 2007) on board the MESSENGER spacecraft has verified the presence of polar deposits on Mercury that exhibit low reflectance, as well as distinct boundaries exhibiting variations in brightness (Chabot et al., 2016). Hamill et al. (2020) delved into the locations and thermal characteristics of these boundaries, revealing that the low-reflectance deposits in these craters spread beyond the PSRs, sometimes extending over 1.0 km.

Table 1
Location, diameter, and maximum depth of Laxness and Fuller craters.

Crater	Location	Diameter	Max depth
Laxness	83.27°N, 50.04°W	27 km	1.8 km
Fuller	82.63°N, 42.65°W	25.9 km	2.4 km

The base topography for the lighting and thermal modeling analyses were derived from DTMs at a resolution of approximately 125 m/px. These DTMs were constructed from MLA track data and reported in Hamill et al. (2020). The generated DTMs include the correction of the orbital geolocation errors by using the track bundle-adjustment method and the photoclinometry techniques was applied to MDIS images to further refine the craters' morphology (Hamill et al., 2020). The topographic profiles for Laxness and Fuller craters, which provide essential details about their structure, are depicted in Fig. 2.

3. Methods

In this section, we will describe the methodology behind our approach, detailing both the illumination and thermal models implemented in our study. The illumination model is designed to simulate the direct and the scattered incidence of light on a crater, accounting for factors such as incidence angle, surface morphology, and reflectivity. This model is crucial for understanding how the solar incidence flux is absorbed, reflected, or transmitted, which in turn influences the thermal behavior of the material. Simultaneously, the thermal model is employed to predict the temperature distribution and heat transfer within the material under study. This model integrates the energy input from the illumination model and considers the material's intrinsic thermal properties like conductivity, specific heat capacity, and density.

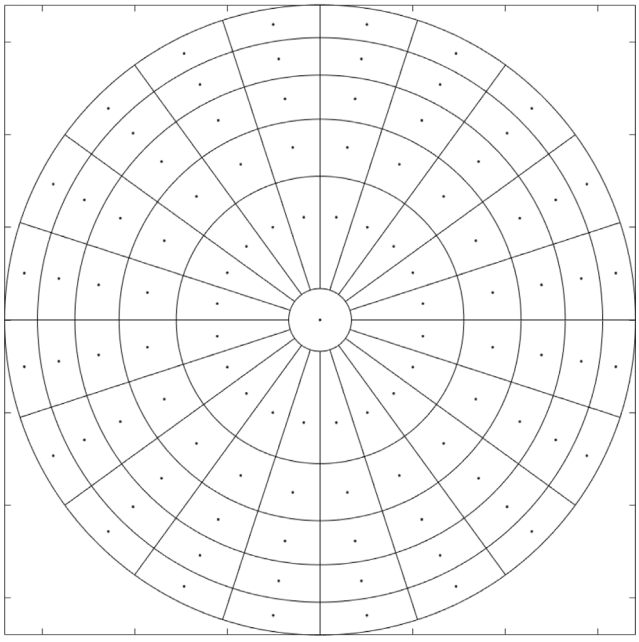

Fig. 3. Discretization of the solar disk into 100 elements. The Sun is uniformly divided into equal solid angles, resulting in a configuration of 5 concentric circles and 20 radial sections. This discretization scheme is used to calculate the visible fraction of the solar disk, taking into account obstructions by the horizon and terrain morphology. The dots represent the centroids of each discretized element.

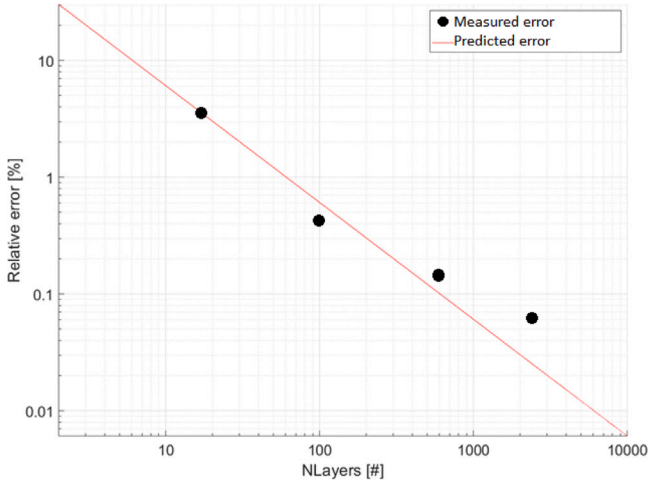

Fig. 4. Relative error of the discretized solar disk as a function of the number of elements (NLayers). The measured error (indicated by black dots) is compared to a high-resolution reference with 10,000 elements, and the predicted quantization error is represented by the red line. The results indicate that a discretization of 100 elements provides sufficient accuracy for our analysis.

We address the complexities introduced by direct illumination, which can cause localized heating and temperature gradients, as well as the diffuse scattering of light, which influences the thermal response of the material. We assume isotropic radiation to ensure a homogeneous and directionally unbiased distribution of radiative energy. The presented thermal model was implemented in Python, and the model's core utilized the finite element method to simulate the temperature changes within the craters over time. We initialized the subsurface temperature matrix and iteratively updated it based on the surface flux data. Our simulation outputs provided a detailed temperature profile for each crater, highlighting the maximum temperature variations that influence the stability of the volatiles within the PSRs.

3.1. Solar illumination: Sun discretization

In order to understand the role of scattering in the thermal behavior of craters at Mercury's north pole, we utilized local DTMs with a resolution of 125 m/px (Hamill et al., 2020) as inputs into our solar illumination and thermal model. The DTMs enabled a precise mapping of the solar flux using the ray-tracing technique, essential for our thermal analysis. Ray-tracing is a rendering technique that simulates the path of light and models the effects of its encounters with virtual objects. It produces high-quality images by tracing the path of light rays and accurately simulating the way these rays interact with the surfaces and materials. In the case of Mercury, we treated the Sun as a disk due to the proximity of the planet to the Sun. As mentioned above, the solar disk has an apparent size ranging between 1.15° at aphelion to 1.76° at perihelion (Filacchione et al., 2020), implying that the surface of Mercury is not illuminated with parallel rays, but the apparent size of the solar disk as seen by the surface causes the formation of both shadows and penumbra. The length of the penumbra varies from 2.46 km at the perihelion to 1.5 km at aphelion in the case of a crater's rim of 2 km height placed at latitude of ±80° (Filacchione et al., 2020).

As mentioned in Section 1, the polar regions of Mercury are characterized by incidence angles proximal to 90° since the solar rays are grazing the surface. To derive the visible fraction of the solar disk while accounting for obstructions caused by the horizon and terrain morphology, we discretized the Sun into 100 elements. Initially, we conducted simulations with varying configurations ranging from 100 to 10,000 elements. Our results demonstrate that a discretization using 100 elements is sufficient for accurate representation (see Fig. 3). As shown in Fig. 4, we achieved a relative accuracy below 1% by adopting a layered approach consisting of 100 elements, structured into 5 concentric rings, each subdivided into 20 angular sectors. Considering that the solar disk is uniformly divided into equal solid angles, the error introduced by discretizing the Sun's source into a finite number of layers can be quantified as a quantization error with a mean square error (MSE) equal to $\delta^2/12$, where δ is the size of a single layer. Having considered the Sun as a disk makes shadow and penumbra modeling more complete in terms of heat flux calculation, since the actual morphology of a crater strongly affects the final amount of insolation received from a geometry element. Illumination conditions are modeled over a period of 176 Earth-days, with a time step of 12 h. The selected time period stems from the Mercury's 3:2 spin–orbit resonance, i.e. the planet rotates three times about its spin axis for every two orbits around the Sun. This time period ensures that the received illumination conditions both at the beginning and at the end are similar. This allows to run the thermal modeling as many times are required to stabilize the temperature, using the thermal map of the end of the first iteration as an input for the next iteration.

3.2. Sunlight scattering and self-heating

Diffuse radiation is responsible for the illumination of areas on the body surface that are shadowed in direct light. This results in the self-heating of the surface by self-thermal emission. In fact, each subfacets of the geometry can absorb thermal radiation from surrounding visible facets and the colder subfacets can be heated by the hotter ones. In order to include the scattering and diffusion of the light in the illumination model, we consider a subfacet i of the crater mesh. Following Yu and Ip (2021), the amount of light leaving the subfacet i can be estimated via

$$L_{tot} = A_i L(i), \tag{1}$$

where A_i is the area of the subfacet i and $L(i)$ is the total light incident onto the facet. Considering i and j two distinct subfacets of the

geometry, the scattering light leaving from surrounding visible facets can be expressed as:

$$L_{scattered}(i) = \sum_{j \neq i} f(i,j) A_i L(j), \tag{2}$$

where $f(i,j)$ is the view-factor (Lagerros, 1998). This factor represents the fraction of radiative energy received by facet i from facet j assuming a Lambertian energy distribution, and can be expressed as:

$$f(i,j) = v_{i,j} a_j \frac{\cos\theta_i \cos\theta_j}{\pi d_{i,j}^2}, \tag{3}$$

if $j \neq i$. On the contrary, if $j = i$, the view-factor is zero. In Eq. (3), $v_{i,j}$ represents the fraction of area that is visible to each other, a_j if the area of facet j, θ_i is the incidence angle on facet i, θ_j is the emission angle from facet j, and $d_{i,j}$ is the distance between the two subfacets. Then, assuming that the subfacet i has a temperature T_i, which was previously calculated in the case of direct light, and that the emission follows a Lambertian law, the integrated thermal radiation absorbed by the subfacet i can be estimated via

$$R_{th}(i) = (1 - A_{th}) \sum_{i \neq j} f(i,j) \epsilon \sigma T_j^4, \tag{4}$$

from the surrounding visible subfacets. In the above equation, A_{th} is the albedo and σ is the Stefan–Boltzmann constant.

3.3. Thermal model

The surface temperature of Mercury is primarily governed by the amount of solar radiation it receives. This energy input is balanced by radiative losses and thermal conduction processes. Understanding this processes is crucial for interpreting observational data and modeling the Mercury's thermal behavior over time. The thermal conduction flux is governed by the following heat conduction equation:

$$\rho(z) c_p(T) \frac{dT}{dt} = \frac{d}{dz}\left[k(T)\frac{dT}{dz}\right], \tag{5}$$

where ρ is the density, c_p is the specific heat capacity, and k is the thermal conductivity. Eq. (5) encapsulates the interplay between different thermal properties and mechanisms. The left term describes the rate of change of thermal energy per unit volumes. It indicates how quickly the temperature of the material changes over time, which depends on the material's density and specific heat capacity. The right term of Eq. (5) represents the heat flux due to conduction and shows how the heat flux changes along the spatial coordinate z. However, radiative energy exchange also plays a critical role in determining Mercury's surface temperature, especially given its proximity to the Sun. The radiative balance can be described considering the spectral distribution of thermal radiation and the material's emissivity. The temperature, which accounts for the total energy radiated across all wavelengths, is given by the following equation:

$$\sigma T^4 = \pi \int_0^\infty \epsilon(\lambda) B(\lambda, T_s) d\lambda = S_0(1 - A), \tag{6}$$

where:

- σ the Stefan–Boltzmann constant,
- T is the temperature,
- $\epsilon(\lambda)$ is the spectral emissivity, which may vary with wavelength,
- S_0 is the solar constant,
- A is the surface albedo.

This equation describes how the surface of Mercury radiates energy across all wavelengths. Together, the conduction equation (Eq. (5)) and the radiative balance equation describe the energy exchange processes that determine Mercury's surface temperature.

3.3.1. Thermophysical parameters and initial conditions

In this study, we investigate the thermophysical properties of a given material by examining its density, specific heat capacity, and thermal conductivity as functions of depth and temperature. Vasavada et al. (2012) and Mitchell and De Pater (1994) show a non-linear dependency of such parameters on either temperature and/or depth. The thermophysical properties are described in the following equations:

- **Density** (ρ) as a function of depth (z) is modeled by an exponential function to consider the surface as two different layers and capture the increase in density with increasing depth, represented by the equation:

$$\rho(z) = \rho_{bottom} - (\rho_{bottom} - \rho_{top}) exp(-z/H) \tag{7}$$

  where ρ is in kg/m^3 and z is in meters. ρ_{bottom} = 1800 kg/m^3 and ρ_{top} = 1300 kg/m^3. The H-parameter describes the vertical trend of the thermal properties of the regolith, within the upper few centimeters (Hayne et al., 2017; Piqueux et al., 2016). Large values of the H-parameter correspond to more insulating material near the surface, and small values correspond to denser, more conductive material. A typical value for the H-parameter is 6 cm (Hayne et al., 2017).
- **Specific heat capacity** ($c_p(T)$) as a function of temperature (T) is modeled as

$$c_p(T) = 0.2029 + 0.0383\left[-exp\left(-\frac{T - 350}{100}\right)\right], \tag{8}$$

  where T is the temperature in K. This expression of the temperature dependent specific heat capacity is valid for extreme Hermean surface temperatures (> 700 K at the subsolar point, Ledlow et al., 1992).
- **Thermal conductivity** ($k(T)$) is modeled as shown in Vasavada et al. (1999) and has the form $k(T) = K_c[1 + \chi(T/350)^3]$, where k_c is the solid conductivity, and χ is the ratio of radiative to solid conductivity at a temperature of 350 K. The top layer of the geometry has the value of the lunar regolith sample from Apollo 12, $K_c = 9.22 \cdot 10^{-4}$ W/m K, and $\chi = 1.48$ (Cremers et al., 1971). The bottom layer has $K_c = 9.3 \cdot 10^{-3}$ W/m K and $\chi = 0.073$ (Mitchell and De Pater, 1994).

We initialized our model with an initial temperature of 300 K (Vasavada et al., 1999).

3.3.2. Boundary conditions

Eq. (5) must be supplemented by heat flux boundary conditions. We consider homogeneous Neumann boundary conditions on the lateral boundaries of the domain Ω. In this case the heat flux can be expressed by Fourier's law of heat conduction as

$$q_s = -k\frac{dT(0,t)}{dx} \tag{9}$$

where q_s is the total heat flux density at surface in W/m^2, k is the thermal conductivity, and dT/dx is the temperature gradient. On the top of the domain Ω, the inward heat flux is specified as:

$$-\mathbf{n} \cdot \mathbf{q} = q_0. \tag{10}$$

In the latter equation $\mathbf{q}$ is the conductive heat flux vector in W/m^2 ($q = -k\nabla T$, where k is the thermal conductivity and T the temperature), $\mathbf{n}$ is the normal vector on the boundary, and q_0 is the inward heat flux in W/m^2 normal to the boundary. The direct solar insolation is defined as

$$q(\mathbf{x}, t) = f_{sun}\frac{S_0 cos(i) \cdot (1 - A)}{R^2}, \tag{11}$$

where S_0 is the solar irradiance (9116,4 W/m^2), R is the mesh element's distance from the Sun in AU, and A is the surface albedo (Gläser and Gläser, 2019). The values for the incidence angle (i) and the dis-

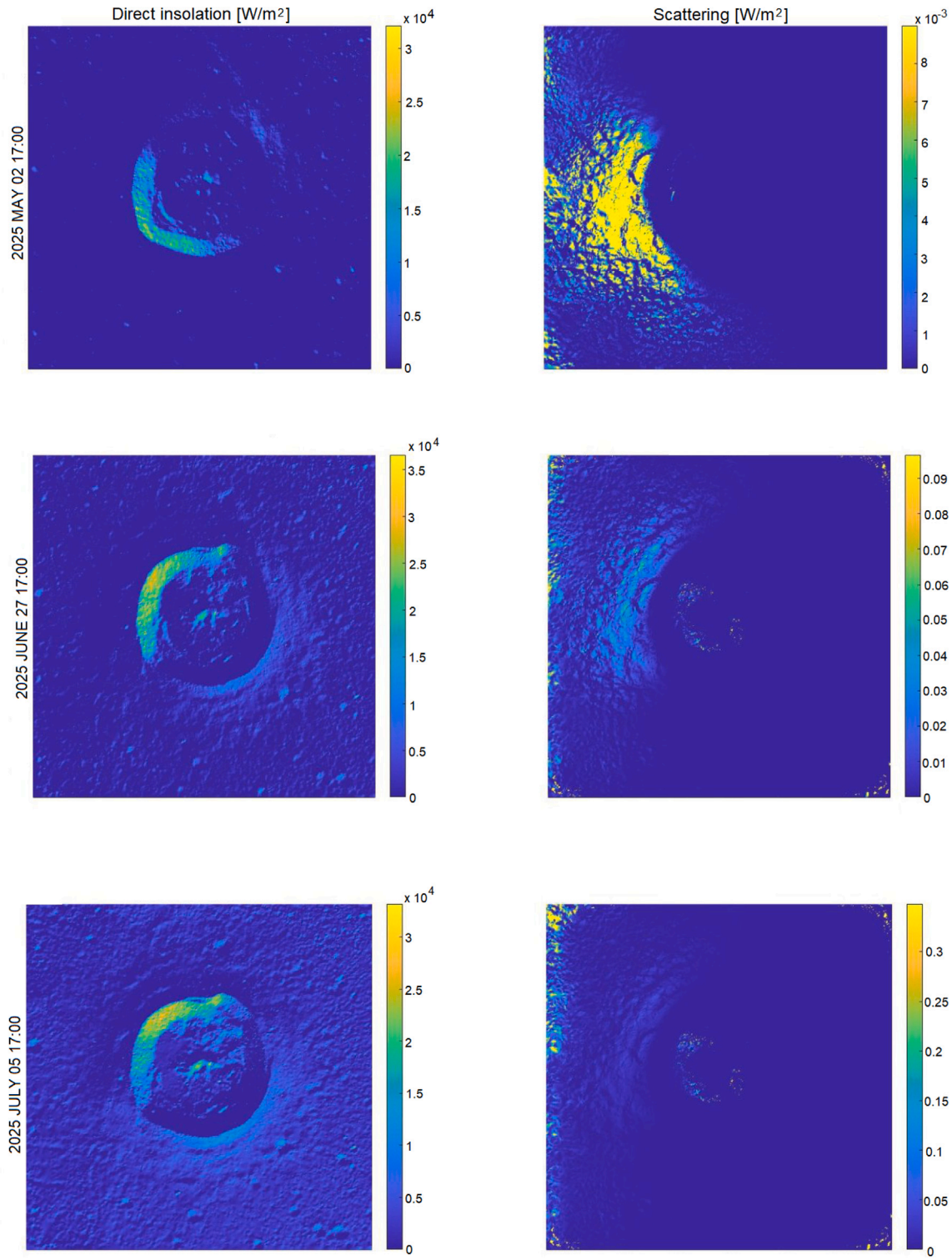

Fig. 5. Direct (left panel) and scattered (right panel) solar flux in the case of the Fuller crater. These illustrations represent selected examples from the simulations conducted over a period of 176 Earth-days.

tance (R) were supplied by the NAIF SPICE toolkit (Acton, 1996). This illumination model treated the Sun as a disk and not as a point source due to the proximity of Mercury to the Sun. For this reason in Eq. (11), $f_{sun} = f_{sun}(\mathbf{x}, t)$ is the visible fraction of the solar disk taking into account solar obstructions by the horizon as seen from the respective location $\mathbf{x}$ at time t. Finally, the constant internal heat flux at the bottom boundary layer is assumed to be 0.020 W/m^2 (Schubert et al., 1988).

4. Method validation

To validate our method, we employ a twofold approach. First, we examine the impact of discretizing the solar disk on the thermal behavior of Mercury's polar craters by comparing results obtained with and without solar discretization. This comparison will help us understand the influence of considering the Sun as an extended source

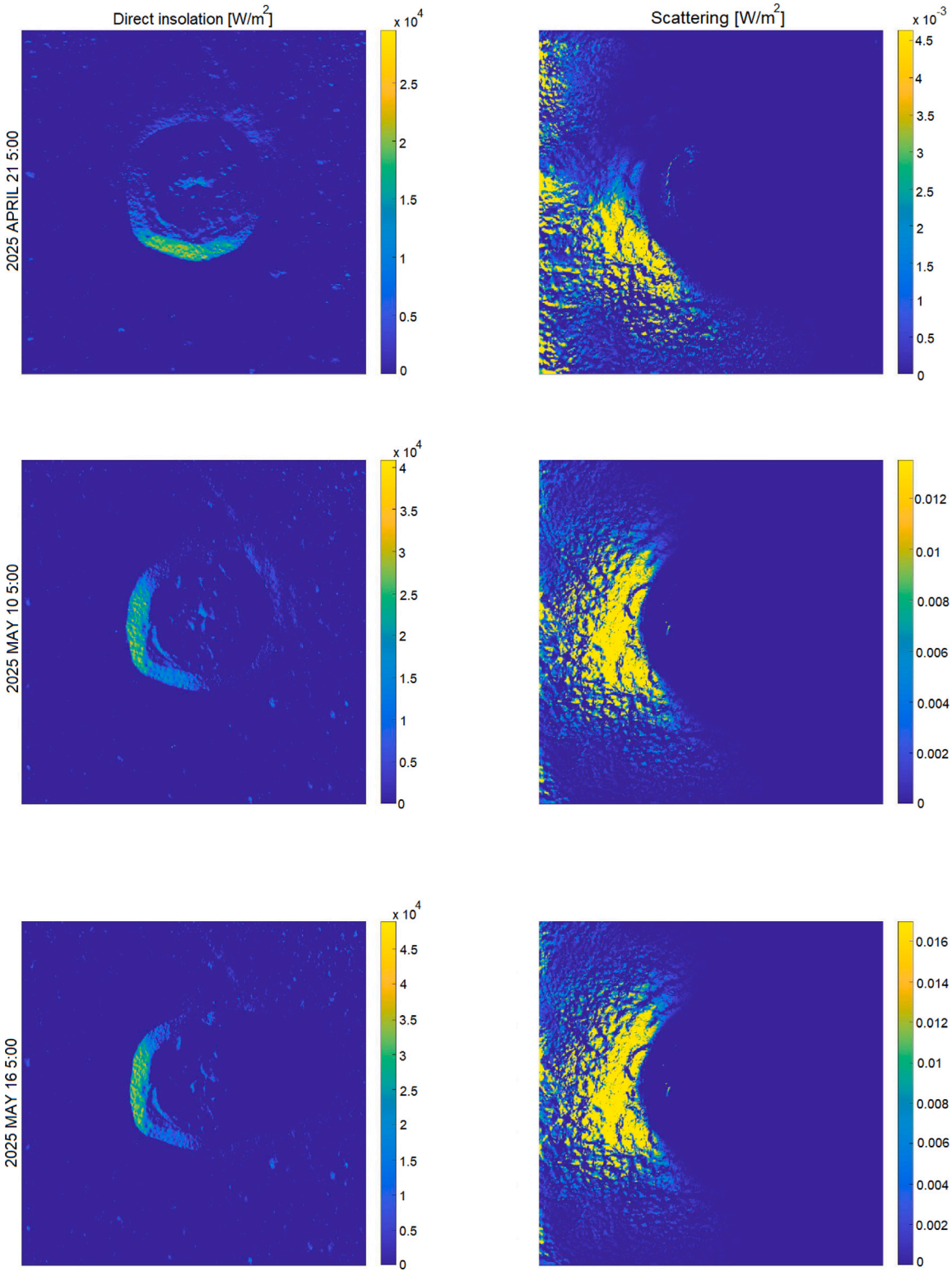

Fig. 6. Direct (left panel) and scattered (right panel) solar flux in the case of the Laxness crater. These illustrations represent selected examples from the simulations conducted over a period of 176 Earth-days.

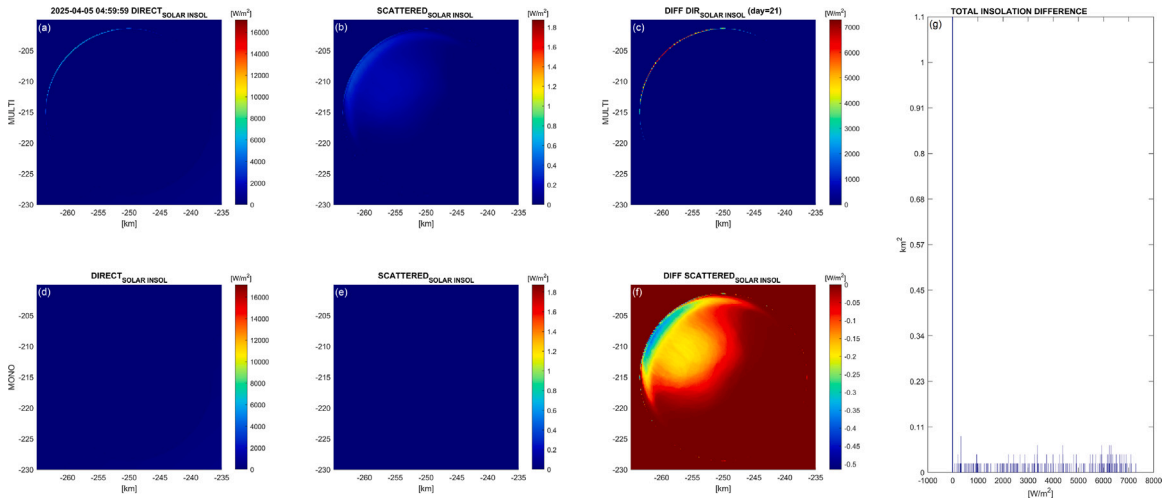

Fig. 7. Analysis and quantification of the effect of solar discretization on the modeled solar insolation. The top row of panels (a, b, c) shows results for the extended source case, while the bottom row (d, e, f) corresponds to the point source scenario. Panels (a) and (d) represent the crater illuminated only by direct solar radiation. Panels (b) and (e) show the effects of scattered light. Panel (c) depicts the variation in W/m^2 between the extended and point source models for direct illumination, and panel (f) shows the difference for the scattered light scenario. The two images represent frames extracted from the 176 day simulation, highlighting the importance of considering the Sun as an extended source. Panel (g) displays a histogram indicating the surface area of the crater in km^2 (y-axis) and the corresponding insolation difference in W/m^2 (x-axis) between the single-source and multi-source models, combining both direct and scattered light contributions.

rather than a point source on the modeled radiance maps. Second, we apply our method to a crater with a known bowled shape and compare the results with published data. This comparison serves as a benchmark to ensure the accuracy and reliability of our thermal model in reproducing observed thermal behaviors of similar craters documented in the literature.

4.1. Assessment of solar discretization effects

As shown in our methodology, we discretized the solar disk into 100 elements to accurately simulate solar illumination on complex topographies, such as Mercury's polar craters. This discretization was achieved by dividing the solar disk into 5 concentric rings, each further subdivided into 20 angular sectors, ensuring a uniform distribution of solid angles. This approach is particularly important due to Mercury's proximity to the Sun, which results in the penumbra effect on the surface (Filacchione et al., 2020). To quantify the importance of the solar discretization, we applied the illumination component of our method to a bowled-shaped crater with the same characteristics (diameter, location, and depth) as the Laxness crater. The first test was conducted without solar discretization, treating the Sun as a point source, and then as an extended source. As shown in Figs. 7 and 8, we present an analysis and quantification of the effect of solar discretization on the modeled solar insolation. The top row of panels (a, b, c) illustrates the results for the extended source case, while the bottom row (d, e, f) corresponds to the point source scenario. Panels (a) and (d) show the crater illuminated only by direct solar radiation, while panels (b) and (e) depict the effects of scattered light. Panel (c) displays the variation in W/m^2 caused by considering either the extended or point source in the case of direct illumination, and panel (f) shows the difference for the scattered light scenario. The two images represent only two frames extracted from the 176 day simulation. What is clearly evident from the images is that discretizing the Sun and considering it as an extended source has a significant effect on the formation of the penumbra. In the case of Fig. 7, panel (a) shows the presence of a thin directly illuminated strip, which is precisely the penumbra, whereas it is completely lost in panel (d). Similarly, in the scattering scenario, it is evident (panel b) that part of the crater is illuminated indirectly, which is not observed in the case of the point source (panel e). Panel (c) shows that, in some areas of the penumbra, the difference in direct insolation between the two cases leads to variations of up to 7000 W/m^2, an increase that can also be observed, albeit to a lesser extent, in the scattering case. The same trend is evident in 8, where, particularly in the case of direct insolation (panels a and d), the penumbra transition observed in panel (a) is completely lost in panel (d), representing the point source scenario. In both cases, the histogram in panel (g) shows the difference in illumination computed using the single-source or multi-source model. In particular, it indicates the crater surface area in km^2 (y-axis) affected by the variation and the corresponding insolation difference in W/m^2 (x-axis).

4.2. Case study: Bowled-shaped crater analysis

The thermal behavior of bowl-shaped craters on airless bodies such as Mercury is heavily influenced by their geometry, as documented by Ingersoll et al. (1992). In their study, the authors modeled craters using a bowl-shaped geometry, which varies based on the crater diameter. For craters with diameters less than 15 km, the depth-to-diameter ratio is approximately 0.2, as derived from empirical studies of fresh lunar craters (Anon., 0000). This ratio is characteristic of younger and deeper craters, which possess steep walls and a more confined geometry. This depth causes most of the crater's interior to remain in shadow, especially in polar regions, where sunlight enters at grazing angles. As a result, the shadowed areas of these craters tend to have low equilibrium temperatures, as direct solar illumination is minimal and primarily restricted to the crater walls. Ingersoll et al. (1992) computed that the temperature in the shadowed regions of these smaller craters can reach as low as 102 K. For craters with diameters greater than 15 km, the depth-to-diameter ratio decreases following a power law. In our study, we observe a temperature of 100.51 K for craters with diameters less than 15 km, which aligns closely with the theoretical prediction of 102 K provided by Ingersoll et al. (1992). For craters larger than 15 km, while no specific theoretical value is available, Ingersoll et al. (1992) suggested that the temperature should decrease due to the smaller depth/diameter ratio, which results in less shadowing and lower equilibrium temperatures in the shadowed regions. Our model predicts a temperature of 91.92 K for these larger craters, consistent with the theoretical expectation of a lower temperature. Furthermore, for flat surfaces, Ingersoll et al. (1992) calculated a temperature of 165 K under polar conditions, where the surface receives more direct sunlight. Our model predicts a similar temperature of 162.94 K, in line with (Paige et al., 2013), demonstrating the consistency and reliability

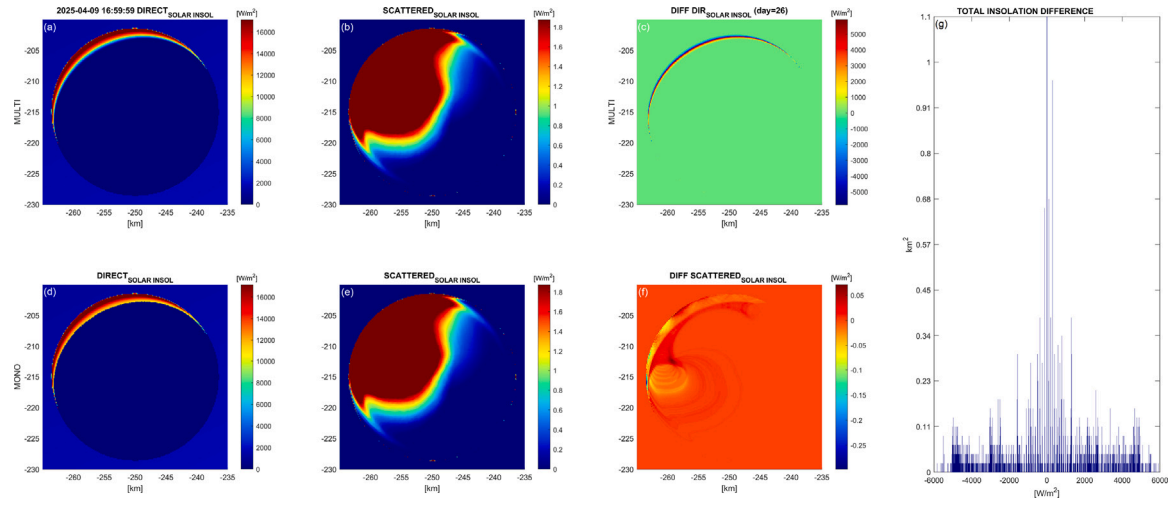

Fig. 8. Analysis and quantification of the effect of solar discretization on the modeled solar insolation. The top row of panels (a, b, c) shows results for the extended source case, while the bottom row (d, e, f) corresponds to the point source scenario. Panels (a) and (d) represent the crater illuminated only by direct solar radiation. Panels (b) and (e) show the effects of scattered light. Panel (c) depicts the variation in W/m^2 between the extended and point source models for direct illumination, and panel (f) shows the difference for the scattered light scenario. The two images represent frames extracted from the 176 day simulation, highlighting the importance of considering the Sun as an extended source. Panel (g) displays a histogram indicating the surface area of the crater in km^2 (y-axis) and the corresponding insolation difference in W/m^2 (x-axis) between the single-source and multi-source models, combining both direct and scattered light contributions.

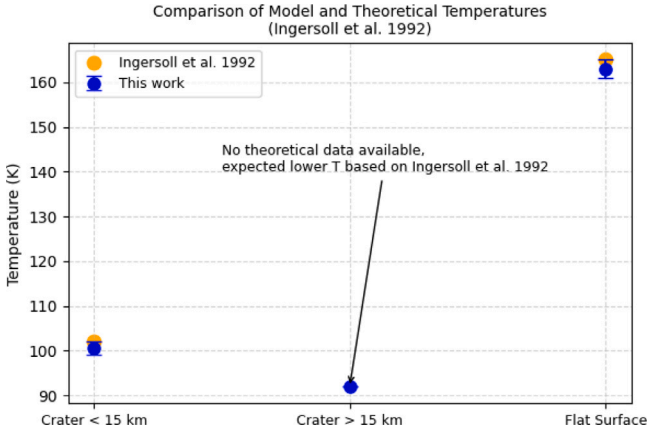

Fig. 9. Comparison between the temperatures obtained in this study (blue points) and the theoretical values from Ingersoll et al. (1992) (orange points) for different crater sizes and flat surfaces. The error bars on the model data indicate the deviation from theoretical predictions.

of our thermal model in replicating theoretical predictions. In Fig. 9, the comparison of the surface temperatures predicted by our thermal model with the theoretical values provided by Ingersoll et al. (1992) for various surface types on Mercury is shown.

5. Results

In Figs. 5 and 6, an example of how scattering affects the dispersion of energy received by the crater's surface is illustrated. On the left, the direct radiation in W/m^2 at a specific epoch can be observed, having simulated a period of 176 Earth-days, while on the right, the areas of the crater where radiation is scattered are highlighted. These results were obtained using a custom tool we developed, which incorporates the discretization of the Sun to accurately model the scattering effects. As can be seen, there are regions that are impacted by solar flux through indirect insolation, due to the craters' morphology. In order to understand how scattering affects the crater's temperature, particularly in the permanently shadowed regions, we calculated the temperature variation over the same time range. We focus our results on the shadowed areas because they represent a peculiar region of the crater and allow us to comprehend the influence of self-heating in areas only heated by scattered radiation. Two examples of maximum temperature profiles for the Laxness and Fuller craters are presented, respectively, in Fig. 10. To extract such profiles, we developed a tool that, after generating the heat map of the crater, allows for the selection of any desired profile in any direction. The tool then extracts the temperature profile along the chosen line. This process results in a plot where the x-axis represents the crater section and the y-axis represents the temperature (see Fig. 10). This approach enables us to analyze temperature variations for each pixel along the selected profile, providing detailed insights into the thermal behavior of different regions within the crater. Additionally, in Fig. 10 the permanently shadowed regions (highlighted in gray) are indicated to enable accurate selection of the profile and facilitate the comparison with areas affected by direct radiation, while the orange box defines the boundaries of the radar-bright material (RBM).

These two examples illustrate the behavior of temperature within PSRs affected by scattering. There is a noticeable increase in temperature greater than what is observed in areas that receive direct illumination. To better quantify this effect, we averaged the maximum temperature variation between the two scenarios and calculated the percentage variation over the 176 Earth-days. For Laxness we found that the data cluster around the 15% average variation. On the contrary, the Fuller crater exhibits values around the 10% average variation. Each measure corresponds to a single day's maximum temperature variation within the PSRs. Moreover, we observe a predominant influence of self-heating mechanisms over the effects of topographic self-illumination. This phenomenon can be attributed to the inherent thermal properties of the crater's surface and the absorptive characteristics of its materials. As shown in Paige et al. (2013), the thermal model calculations combined with radar measurements suggest that Mercury's polar deposits are composed dominantly of water ice. At the considered latitudes, the temperature at which a water ice deposit can be considered thermally stable depends on the time scale under consideration (Paige et al., 2013). At a temperature of 102 K, for instance, a meter-thick layer of pure water ice would sublimate in 1 billion years, whereas at a temperature of 210 K, it would sublimate in 35 days. As shown in Fig. 10, self-heating does not affect the stability of water ice in the Laxness crater. However, in the case of the Fuller

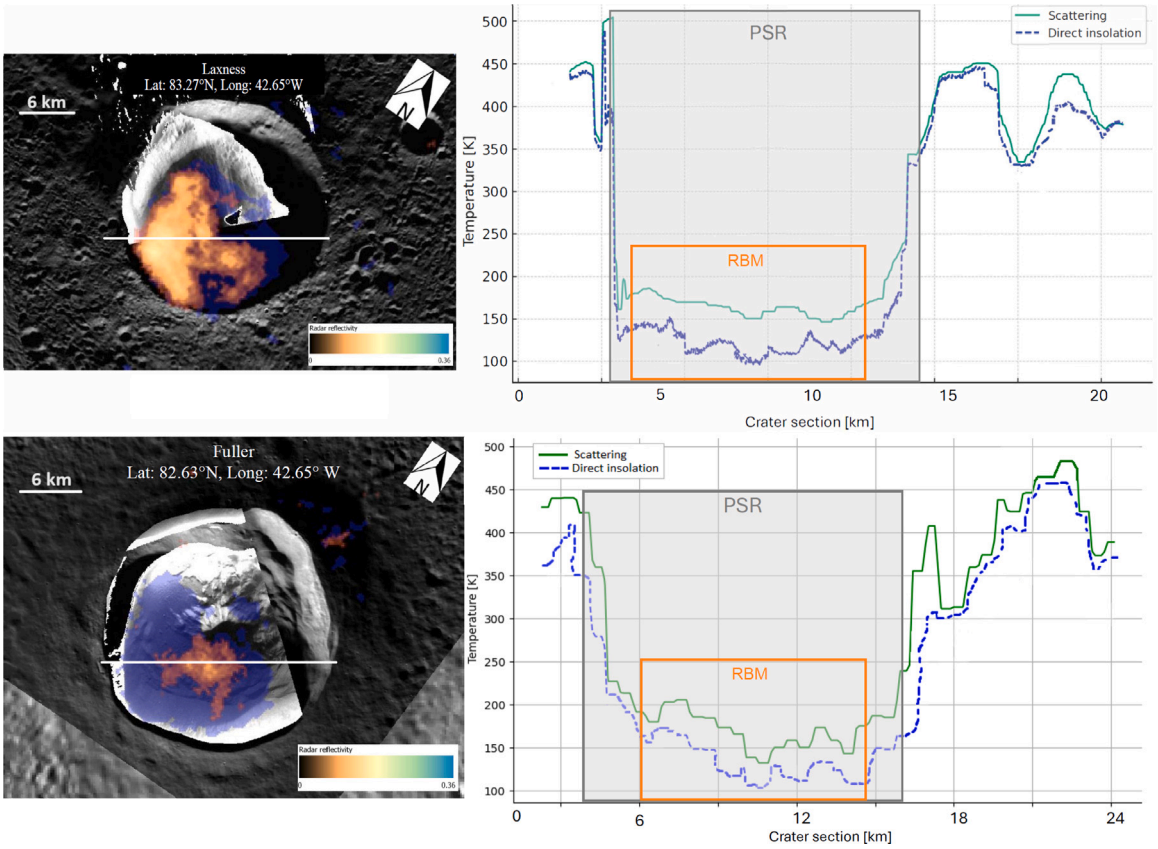

Fig. 10. Temperature profile of the Laxness (top) and Fuller (bottom) crater's interior. On the left, the regions within the crater that are permanently shadowed (blue) and the radar bright material (orange) against the crater's topography are highlighted. The right side of the image illustrates a comparative analysis of daily maximum temperatures within the crater. The green line indicates temperatures under scattered light conditions, while the blue dashed line represents temperatures experienced during direct sunlight exposure. The gray box represents the boundaries of the PSRs. The orange box defines the boundaries of the radar bright material (RBM).

crater, while most areas remain stable, a section within the radar-bright material reaches temperatures of up to 210 K due to self-heating. Although the thickness of this ice layer is unknown, it will be intriguing to revisit this target with the upcoming BepiColombo mission and the SIMBIO-SYS instrument to better understand the current state of this crater.

6. Conclusions

In this study, we have quantified the thermal impact of scattering and self-heating on temperature distributions within Mercury's north polar craters, specifically focusing on the Laxness and Fuller craters. Our approach involved the development of a custom tool designed to discretize the Sun, which is critical for accurately modeling the influence of solar illumination on Mercury's surface. Unlike previous studies that often treated the Sun as a point source, our method discretized the Sun into 100 elements, allowing for a more precise simulation of the solar flux, particularly in regions where the Sun's apparent size has a significant impact, such as the polar regions. The application of this tool to high-resolution DTMs enabled us to generate detailed illumination maps and temperature profiles, which revealed the complex interplay between solar illumination, scattering, and the thermal responses of surface materials. Our findings highlighted the significant role of scattering in elevating temperatures within PSRs, often exceeding those in areas of direct illumination. This underscores the non-negligible impact of self-heating in these regions, which, while not destabilizing volatiles in the Laxness crater, does push the temperature within a section of the Fuller crater's radar-bright material to near 210 K. Although the exact thickness of the ice layer within these regions remains unknown, our results suggest that further investigation is necessary. The upcoming BepiColombo mission, with its advanced instruments such as the SIMBIO-SYS, offers an exciting opportunity to revisit these craters and gain a deeper understanding of their current thermal state. This future research will be pivotal in refining our models and ensuring that we can accurately predict the stability of volatiles in Mercury's challenging polar environments.

CRediT authorship contribution statement

Pamela Cambianica: Writing – original draft, Validation, Supervision, Software, Methodology, Investigation, Conceptualization. **Emanuele Simioni:** Writing – review & editing, Software, Methodology. **Gabriele Cremonese:** Writing – review & editing, Supervision, Project administration, Funding acquisition. **Silvia Bertoli:** Writing – review & editing, Data curation. **Elena Martellato:** Writing – review & editing, Validation. **Alice Lucchetti:** Writing – review & editing. **Maurizio Pajola:** Writing – review & editing. **Cristina Re:** Writing – review & editing. **Adriano Tullo:** Writing – review & editing. **Matteo Massironi:** Writing – review & editing.

Declaration of competing interest

The authors declare that they have no known competing financial interests or personal relationships that could have appeared to influence the work reported in this paper.

Acknowledgments

We gratefully acknowledge funding from the Italian Space Agency (ASI) under ASI-INAF agreement 2017- 47-H.0.

Data availability

Data will be made available on request.

References

Acton, Jr., C.H., 1996. Ancillary data services of NASA's navigation and ancillary information facility. Planet. Space Sci. 44 (1), 65–70.

Anon., 0000. Depth/diameter relations of fresh lunar craters: Revision from spacecraft data. GRL 1 (7), 291–294.

Benkhoff, J., Murakami, G., Baumjohann, W., Besse, S., Bunce, E., Casale, M., et al., 2021. BepiColombo-mission overview and science goals. Space Sci. Rev. 217 (8), 90.

Buhl, D., Welch, W.J., Rea, D.G., 1968. Reradiation and thermal emission from illuminated craters on the lunar surface. J. Geophys. Res. 73 (16), 5281–5295.

Butler, B., Muhleman, D., Slade, M., Jurgens, R., 1991. Mercury goldstone/VLA radar: Part II. In: Bulletin of the American Astronomical Society, vol. 23. p. 1200.

Capaccioni, F., De Sanctis, M.C., Filacchione, G., Doressoundiram, A., Erard, S., Hello, Y., et al., 2009. The visible and infrared hyperspectral imager (VIHI) of the BepiColombo MPO mission: Development status and observation strategy. In: EGU General Assembly Conference Abstracts. p. 12214.

Cavanaugh, J.F., Smith, J.C., Sun, X., Bartels, A.E., Ramos-Izquierdo, L., Krebs, D.J., et al., 2007. The mercury laser altimeter instrument for the MESSENGER mission. Space Sci. Rev. 131, 451–479.

Chabot, N.L., Ernst, C.M., Denevi, B.W., Nair, H., Deutsch, A.N., Blewett, D.T., et al., 2014. Images of surface volatiles in Mercury's polar craters acquired by the MESSENGER spacecraft. Geology 42 (12), 1051–1054.

Chabot, N.L., Ernst, C.M., Paige, D.A., Nair, H., Denevi, B.W., Blewett, D.T., et al., 2016. Imaging mercury's polar deposits during MESSENGER's low-altitude campaign. Geophys. Res. Lett. 43 (18), 9461–9468.

Cremers, C.J., Birkebak, R.C., White, J.E., 1971. Lunar surface temperatures from Apollo 12. Moon 3 (3), 346–351.

Cremonese, G., Capaccioni, F., Capria, M.T., Doressoundiram, A., Palumbo, P., Vincendon, M., et al., 2020. SIMBIO-SYS: Scientific cameras and spectrometer for the BepiColombo mission. Space Sci. Rev. 216, 1–78.

Cremonese, G., Fantinel, D., Giro, E., Capria, M.T., Deppo, V.da., Naletto, G., et al., 2009. The stereo camera on the BepiColombo ESA/JAXA mission: A novel approach. In: Advances in Geosciences, vol. 15, Planetary Science (PS), pp. 305–322.

Deutsch, A.N., Chabot, N.L., Mazarico, E., Ernst, C.M., Head, J.W., Neumann, G.A., Solomon, S.C., 2016. Comparison of areas in shadow from imaging and altimetry in the north polar region of mercury and implications for polar ice deposits. Icarus 280, 158–171.

Deutsch, A.N., Head, J.W., Chabot, N.L., Neumann, G.A., 2018. Constraining the thickness of polar ice deposits on Mercury using the mercury laser altimeter and small craters in permanently shadowed regions. Icarus 305, 139–148.

Deutsch, A.N., Neumann, G.A., Head, J.W., 2017. New evidence for surface water ice in small-scale cold traps and in three large craters at the north polar region of Mercury from the Mercury laser altimeter. Geophys. Res. Lett. 44 (18), 9233–9241.

Durga Prasad, K., Rai, V.K., Murty, S.V.S., 2022. A comprehensive 3D thermophysical model of the lunar surface. Earth Space Sci. 9 (12), e2021EA001968.

Filacchione, G., Frigeri, A., Raponi, A., Ciarniello, M., Capaccioni, F., De Sanctis, M.C., et al., 2020. Temporal evolution of the permanent shadowed regions at mercury poles: Applications for spectral detection of ices by SIMBIOSYS-VIHI on BepiColombo mission. Mon. Not. R. Astron. Soc. 498 (1), 1308–1318.

Formisano, M., De Sanctis, M.C., De Angelis, S., Carpenter, J.D., Sefton-Nash, E., 2019. Prospecting the Moon: Numerical simulations of temperature and sublimation rate of a cylindric sample. Planet. Space Sci. 169, 8–14.

Formisano, M., Federico, C., De Sanctis, M.C., Frigeri, A., Magni, G., Raponi, A., Tosi, F., 2018. Thermal stability of water ice in Ceres' craters: The case of Juling crater. J. Geophys. Res. Planets 123 (9), 2445–2463.

Gläser, P., Gläser, D., 2019. Modeling near-surface temperatures of airless bodies with application to the Moon. Astron. Astrophys. 627 (A129).

Hall, K., Thorn, C.E., 2014. Thermal fatigue and thermal shock in bedrock: An attempt to unravel the geomorphic processes and products. Geomorphology 206, 1–13.

Hamill, C.D., Chabot, N.L., Mazarico, E., Siegler, M.A., Barker, M.K., Camacho, J.M.M., 2020. New illumination and temperature constraints of Mercury's volatile polar deposits. Planet. Sci. J. 1 (3), 57.

Harmon, J.K., Slade, M.A., Rice, M.S., 2011. Radar imagery of mercury's putative polar ice: 1999–2005 Arecibo results. Icarus 211 (1), 37–50.

Hawkins, S.E., Boldt, J.D., Darlington, E.H., Espiritu, R., Gold, R.E., Gotwols, B., et al., 2007. The Mercury dual imaging system on the MESSENGER spacecraft. Space Sci. Rev. 131, 247–338.

Hayne, P.O., Bandfield, J.L., Siegler, M.A., Vasavada, A.R., Ghent, R.R., Williams, J.P., et al., 2017. Global regolith thermophysical properties of the Moon from the diviner lunar radiometer experiment. J. Geophys. Res. Planets 122 (12), 2371–2400.

Ingersoll, A.P., Svitek, T., Murray, B.C., 1992. Stability of polar frosts in spherical bowl-shaped craters on the Moon, Mercury, and Mars. Icarus 100 (1), 40–47.

Jamsa, S., Peltoniemi, J.I., Lumme, K., 1993. Thermal emission from a rough surface: Ray optics approach. Astron. Astrophys. 271 (319).

Lagerros, J.S., 1998. Thermal physics of asteroids. IV. Thermal infrared beaming. Astron. Astrophys. 332, 1123–1132.

Ledlow, M.J., Burns, J.O., Gisler, G.R., Zhao, J.H., Zeilik, M., Baker, D.N., 1992. Subsurface emissions from mercury-VLA radio observations at 2 and 6 centimeters. Astrophys. J. Part 1 (ISSN: 0004-637X) 384, 640–655.

Mitchell, D.L., De Pater, I., 1994. Microwave imaging of mercury's thermal emission at wavelengths from 0.3 to 20.5 cm. Icarus 110 (1), 2–32.

Molaro, J., Byrne, S., 2012. Rates of temperature change of airless landscapes and implications for thermal stress weathering. J. Geophys. Res. Planets 117 (E10).

Neumann, G.A., Cavanaugh, J.F., Sun, X., Mazarico, E.M., Smith, D.E., Zuber, M.T., et al., 2013. Bright and dark polar deposits on mercury: Evidence for surface volatiles. Science 339 (6117), 296–300.

Paige, D.A., Siegler, M.A., Harmon, J.K., Neumann, G.A., Mazarico, E.M., Smith, D.E., et al., 2013. Thermal stability of volatiles in the north polar region of Mercury. Science 339 (6117), 300–303.

Paige, D.A., Wood, S.E., Vasavada, A.R., 1992. The thermal stability of water ice at the poles of Mercury. Science 258 (5082), 643–646.

Piqueux, S., Kleinböhl, A., Hayne, P.O., Heavens, N.G., Kass, D.M., McCleese, D.J., et al., 2016. Discovery of a widespread low-latitude diurnal CO2 frost cycle on Mars. J. Geophys. Res. Planets 121 (7), 1174–1189.

Rozitis, B., Emery, J.P., Siegler, M.A., Susorney, H.C.M., Molaro, J.L., Hergenrother, C.W., Lauretta, D.S., 2020. Implications for ice stability and particle ejection from high-resolution temperature modeling of asteroid (101955) Bennu. J. Geophys. Res. Planets 125 (8), e2019JE006323.

Scharringhausen, M., Witte, L., 2020. An efficient and lightweight illumination model for planetary bodies including direct and diffuse radiation. J. Imaging 6 (9), 84.

Schubert, G., Ross, M.N., Stevenson, D.J., Spohn, T., 1988. Mercury's thermal history and the generation of its magnetic field. Mercury 429–460.

Solomon, S.C., McNutt, R.L., Gold, R.E., Domingue, D.L., 2007. MESSENGER mission overview. Space Sci. Rev. 131, 3–39.

Vasavada, A.R., Bandfield, J.L., Greenhagen, B.T., Hayne, P.O., Siegler, M.A., Williams, J.P., Paige, D.A., 2012. Lunar equatorial surface temperatures and regolith properties from the diviner lunar radiometer experiment. J. Geophys. Res. Planets 117 (E12).

Vasavada, A.R., Paige, D.A., Wood, S.E., 1999. Near-surface temperatures on mercury and the Moon and the stability of polar ice deposits. Icarus 141 (2), 179–193.

Wakita, S., Minoru, S., 2011. Thermal evolution of icy planetesimals in the solar nebula. Earth Planets Space 63, 1193–1206.

Watson, K., Murray, B.C., Brown, H., 1961a. The behavior of volatiles on the lunar surface. J. Geophys. Res. 66 (9), 3033–3045.

Watson, K., Murray, B., Brown, H., 1961b. On the possible presence of ice on the Moon. J. Geophys. Res. 66 (5), 1598–1600.

Yu, L.L., Ip, W.H., 2021. Thermophysical model for realistic surface layers on airless small bodies: Applied to study the spin orientation and surface dust properties of (24) themis from WISE/NEOWISE multiepoch thermal light curves. Astrophys. J. 913 (2), 96.

Zusi, M., Paolinetti, R., Corte, V.Della, Marra, G., Baroni, M., Palumbo, P., Cremonese, G., 2019. Optical design of the high resolution imaging channel of SIMBIO-SYS. Appl. Opt. 58 (15), 4059–4069.